Supporting Information

This document contains supporting information for the manuscript "Are cloud radiative effects constrained to cancel over the tropical warm pools?" by Wall et al. Some additional analysis on the differences in climate between the simulations is presented. This is followed by a sensitivity study.

Climates of the Global Radiative-Convective Equilibrium Simulations

In the main manuscript we present two simulations from a global atmosphere model coupled with a slab ocean and run in global radiative-convective equilibrium configuration. A "Control" simulation is performed, and then the SW fluxes at the ocean surface from this simulation are randomized and used to force a "Random SW" simulation. Sea surface temperature (SST) gradients, atmospheric energy transport, and cloud radiative effects (CRE) are compared between the two simulations because these are the key quantities for the hypothesis of Hartmann et al. [2001]. In the discussion that follows we will examine other aspects of the climate in these simulations to further understand the behavior of the model.

a. The Surface Heat Budget and the Regulation of SST

We begin by considering interactions among cloud albedo, atmospheric circulation, and SST, which we call the "cloud-shading feedback." Hartmann et al.

[2001] hypothesized that such interactions could constrain the net CRE within the tropical warm pools. If we are to investigate their hypothesis, then we must first demonstrate that our model realistically simulates the cloud-shading feedback on which the hypothesis is based. We investigate this by examining the covariation between the column-average vertical motion ($\overline{\omega}$), SST anomalies, and the downward SW flux at the ocean surface. SST anomalies are computed by subtracting a 30-day running mean from the data to remove low-frequency fluctuations. High-pass filtering is necessary because SST in the Control climate has a prominent mode of monthly-to-interannual variability with an amplitude of 1-2°C (Figure S1, Coppin and Bony [2017]). We use 30 days for the averaging window because Hartmann et al. [2001] hypothesized that their feedback mechanism must operate on a timescale of several days, and because we wish to compare the Control climate to the observational results of Wall et al. [2018], who used a 30-day averaging window. Our results are not sensitive to modest changes in the length of the averaging window.

To investigate the cloud shading feedback, we define days of moderate-to-strong ascent as those in which $\overline{\omega}$ exceeds one standard deviation in magnitude, and then we identify the times and locations in which the ascending motion reaches its peak value. Lead-lag composites centered on these key days are shown in Figure S2. Between lags of -15 days to -3 days, vertical motion is near zero, SW heating of the ocean is constant, and the SST warms steadily. After this period, ascending motion begins to develop and reaches its peak at lag 0. The strong ascent generates optically thick clouds, which shade the ocean surface and reduce the downward SW flux by

about 90 Wm^{-2} relative to the previous non-convective period. This causes the SST to abruptly cool by several tenths of a degree. The cooling of the SST has a stabilizing effect on the atmosphere above and acts to inhibit further convection. At a lag of +2 days the ascending motion has ceased, and the SST begins to steadily warm under the renewed solar heating. The warming of the SST continues through a lag of +15 days.

The covariation of surface SW flux, $\overline{\omega}$, and SST is consistent with a cloud-shading feedback. Furthermore, the amplitude of the SST fluctuations is about 0.6 °C, which is similar to observed values [Wall et al., 2018]. The timescale of the SST fluctuations, including the relatively abrupt cooling beneath convective clouds with a timescale of ~1-2 days and the slower warming during non-convective conditions with a timescale of ~10 days, agrees with observations to within a factor of two [Wall et al., 2018].

To measure the importance of this feedback mechanism for the regulation of SST, we examine the covariation of SST and the surface heat budget, including the net flux of SW and LW radiation and sensible and latent heat. Anomalies of these terms are computed by removing the 90-day running mean. A longer averaging window is used for this analysis because we wish to compare the Control and Random SW simulations, and the SST anomalies build and decay over a longer timescale in the Random SW simulation, as will be shown shortly. The results are not sensitive to lengthening or shortening the averaging window by a factor of two. A similar lead-lag compositing analysis is performed, except the composites are

centered on the peak of warm SST events, which are defined as warm SST anomalies that exceed one standard deviation in magnitude.

The surface heat budget and SST for the Control simulation are shown in Figure S3a and S3d, respectively. SW heating of the ocean is strongest when the SST is warming (negative lags), and weakest when the SST is cooling (positive lags). The SW heating anomalies are in phase with the SST tendency, indicating that SW heating regulates SST. The fluctuations in SW heating have the largest amplitude of the surface heat flux terms, but evaporative cooling is a non-negligible process that also regulates SST. Fluctuations in LW and sensible heating are relatively small.

The surface heat budget in the Random SW simulation is shown in Figure S3b. In this simulation, SW heating stochastically forces the SST. Even though surface SW heating is random, it still has a relatively large amplitude (~90 Wm^{-2}), so SW anomalies tend to be positive one day before the SST maximum and negative one day after. This stochastic forcing can perturb the SST and initiate other feedbacks, which ultimately regulate the SST. In particular, the latent heating term in Figure S3b has the largest amplitude of the remaining surface heat fluxes, and is especially important for cooling the SST at positive lags, when the warm SST anomaly is decaying. LW heating of the ocean is comparable to latent heating at negative lags, when the warm SST anomaly is building, but less important at positive lags, when the SST anomaly is decaying. Thus, the regulation of SST in the Random SW simulation is accomplished primarily by evaporative cooling. This process is less efficient in regulating SST than cloud shading effects in the Control simulation, as

can be seen by the fact that the peak SST anomaly is twice as large in the Random SW simulation than the Control simulation (cf. Figure S3 d,e).

One may ask if the effect of SW heating in regulating SST has been completely removed in the Random SW simulation, given that SW heating tends to have large amplitude just before and after the peak SST anomaly. To check this, we performed another simulation called "Uniform SW" where the downward SW flux at the ocean surface is constant in space and time and is prescribed to the average value from the Control simulation. In the Uniform SW simulation, the average SW heating of the ocean is identical to that in the Control simulation, but the stochastic forcing of the Random SW simulation is removed. The covariation of latent heat, sensible heat, net LW flux, and SST are all similar between the Random SW and Uniform SW simulations (cf. Figure S3b-c, Figure S3e-f). This indicates that the processes regulating SST are the same whether the cloud shading feedback is removed by randomizing surface SW heating or fixing surface SW heating to a constant value.

The Uniform SW case is also useful in that it allows us to check if other aspects of the simulations are sensitive to the method of removing the cloud-shading feedback, whether it be randomizing or fixing the surface SW heating. Figure S4 shows a comparison of the patterns and statistics of SST anomalies in the Random SW and Uniform SW simulations. The SST patterns are similar in that they both have narrow warm bands surrounded by large SST gradients and broad cold pools. The probability density functions of SST anomalies are also similar in the two simulations. The average SST contrast between rising and sinking regions is 4.1 °C and 4.0 °C in the Random SW and Uniform SW simulations, respectively.

Furthermore, Figure S5 shows the energy transport from ascending regions by the atmospheric circulation in the Random SW and Uniform SW simulations. The distribution of energy transport is very similar between these simulations, and the average energy transport is 79 Wm^{-2} and 77 Wm^{-2} in the Random SW and Uniform SW simulations, respectively. Finally, the net CRE contrast between rising and sinking regions is 29 Wm^{-2} in both the Random SW and Uniform SW simulations. The main conclusions are therefore the same whether the cloud shading feedback is removed by randomizing the surface SW heating or by holding the surface SW heating constant.

b. Characteristics of the Large-Scale Circulation

We have seen that if one removes the mutual interaction between cloud shading effects, SST, and atmospheric circulation, then evaporative cooling becomes the dominant mechanism regulating SST. Evaporative cooling is less efficient in regulating SST, so larger SST gradients are able to develop. We will now investigate the impact this has on the large-scale atmospheric circulation.

We begin with two metrics of the circulation: the near-surface wind speed and the subsidence fraction. The subsidence fraction, which is defined as the fraction of the domain where the column-average vertical motion is downward, is a common metric for the degree of convective aggregation. The global-mean near-surface wind speed is 1.8 m/s larger in the Random SW simulation than in the Control simulation, which is a 53% increase, and the subsidence fraction is about 10% larger in the Random SW simulation (Table S1). Thus, the enhanced SST

gradients in the Random SW simulation substantially speed up the low-level winds and contract the convective regions.

Changes in the circulation are investigated further by considering modes of variability of the vertical pressure velocity, ω, which we calculate by applying principal component analysis to the vertical profile of ω. Data from all times and all locations are used in this analysis, but the data are weighted by the square root of the cosine of latitude and the mass of each vertical level before calculating the principal components. The principal components are then regressed on ω at each level to recover the associated patterns, or empirical orthogonal functions (EOFs). These patterns represent common modes of the vertical structure of ω.

Figure S6 shows the first and second EOFs of ω for the Control and Random SW simulations. In both simulations the first EOF has the same sign throughout the troposphere, while the second EOF changes sign in the middle troposphere. These modes correspond to deep and shallow overturning motion, respectively. Since the EOFs have similar shapes in the two simulations, the two simulations have dominant modes of variability that are similar in their vertical structure. However, the relative importance of two modes, as indicated by the fraction of variance explained by the modes, is significantly different between the two simulations: The deep overturning mode is more prominent and the shallow overturning mode is less prominent in the Random SW simulation compared to the Control simulation (Figure S6). Furthermore, the amplitude of the deep mode is larger in the Random SW simulation than it is in the Control simulation, which indicates that deep ascent tends to be stronger in the Random SW simulation when it occurs.

c. Global-Mean Climate Metrics

We conclude by comparing some global-mean climate metrics between the Control and Random SW simulations, which are listed in Table S1. We have seen that the Random SW simulation has stronger SST gradients, which cause stronger near-surface winds. Because the dominant terms in the surface heat budget are SW heating and evaporative cooling, and because the surface SW heating is identical in the two simulations, one might expect that global-mean evaporative cooling will also be similar between the two simulations. If the surface latent heat flux is to remain constant as the near-surface wind speed increases, then the SST must cool or the near-surface saturation deficit (100% minus the near-surface relative humidity) must decrease. The saturation deficit increases modestly in the Random SW simulation, probably due to the contraction of the moist, convective regions. Therefore, the global-mean SST must cool in the Random SW simulation to compensate for the stronger low-level winds. Indeed, the global-mean SST is 7.2 °C colder in the Random SW simulation.

There are other energetic constraints that prevent the two simulations from having identical surface evaporation rates, however. In the global mean, the surface evaporation rate equals the precipitation rate, and the latent heat released through precipitation must approximately balance the radiative cooling of the atmosphere. The radiative cooling rate of the tropical atmosphere decreases if atmospheric temperatures cool. If we assume that the atmospheric temperature is connected to the SST through a moist adiabatic lapse rate, then cooling of the SST will result in reduced radiative cooling of the atmosphere, and therefore reduced evaporation at

the ocean surface. Furthermore, the contraction of the moist, convective regions in the Random SW simulation allows for more efficient cooling of the ocean surface by LW emission. In the Random SW simulation, the model satisfies all of these constraints by reaching a state with colder SST, reduced precipitation, reduced evaporation from the ocean surface, and enhanced surface LW cooling (Table S1).

Sensitivity Study

To test if our results are robust we repeat the experiments with eight different combinations of free parameters. The depth of the slab ocean model, which controls the timescale of the cloud shading feedback, is varied between 5 m and 30 m, which we chose to match the typical thicknesses of the diurnal warm layer and full mixed layer that are observed in the tropical western Pacific Ocean [Soloviev and Lukas, 1996; Soloviev and Lukas, 2006]. We also vary the magnitude of the uniform heat sink, or "Q flux," that is applied to the slab ocean model. The Q flux is varied by 40 Wm^{-2}, which results in a global-mean SST change of 7.4 °C (Figure S7). We check the sensitivity of the results to global-mean SST because previous studies have suggested that the instability that generates spontaneous convective aggregation critically depends on atmospheric temperature [Emanuel et al., 2014]. Thus, the degree of convective aggregation in the Control simulation could depend on the mean SST, and if so, then perhaps the response to randomizing the surface SW fluxes could also depend on the mean SST. Varying the Q flux allows us to check this.

The results of the sensitivity study are presented in Figure S8. In all experiments the results are similar to those presented in the main text: randomizing the surface SW fluxes leads to substantially larger SST gradients, stronger lateral energy transport by atmospheric motions, a larger net CRE contrast between rising and sinking regions, and a larger subsidence fraction (i.e. convection that is more aggregated). The enhancement in subsidence fraction in the Random SW simulations, which ranges from 5.1% to 10.0%, is much larger than the natural variability of subsidence fraction in the Control experiments, which has a standard deviation of about 1.5%. Furthermore, the correlation between subsidence fraction and global-mean SST is weak or insignificant on monthly timescales ($r = 0.29$ and $r = 0.16$ in Control experiments 3 and 8, which have mixed-layer depths of 5 m and 30 m, respectively). The enhancement in subsidence fraction in the Random SW simulations is therefore mostly due to the enhancement in SST gradients rather than the change in global-mean SST. All experiments in the sensitivity study support the hypothesis of Hartmann et al. [2001]. Thus, our main conclusions are not sensitive to modest changes in global-mean SST or the timescale of the cloud shading feedback.

References

Coppin, D., and Bony, S. (2017), Internal variability in a coupled general circulation model in radiative-convective equilibrium, *Geophys. Res. Lett.*, 44, 5142– 5149, doi:10.1002/2017GL073658.

Emanuel, K., Wing, A. A., & Vincent, E. M. (2014). Radiative-convective instability. *Journal of Advances in Modeling Earth Systems*, *6*(1), 75–90. http://doi.org/10.1002/2013MS000270

Hartmann, D. L., Moy, L. a., & Fu, Q. (2001). Tropical convection and the energy balance at the top of the atmosphere. *Journal of Climate*, *14*(24), 4495–4511. http://doi.org/10.1175/1520-0442(2001)014<4495:TCATEB>2.0.CO;2

Soloviev, A., & Lukas, R. (1996). Observation of Spatial Variability of Diurnal Thermocline and Rain-Formed Halocline in the Western Pacific Warm Pool. *Journal of Physical Oceanography*. http://doi.org/10.1175/1520-0485(1996)026<2529:OOSVOD>2.0.CO;2

Soloviev, A., & Lukas, R. (2006). *The Near-Surface Layer of the Ocean*, pp. 572, Springer, Netherlands.

Wall, C. J., Hartmann, D. L., Thieman, M. M., Smith, W. L., & Minnis, P. (2018). The Life Cycle of Anvil Clouds and the Top-of-Atmosphere Radiation Balance over the Tropical West Pacific. *Journal of Climate*, *31*(24), 10059–10080. http://doi.org/10.1175/JCLI-D-18-0154.1

Tables and Figures

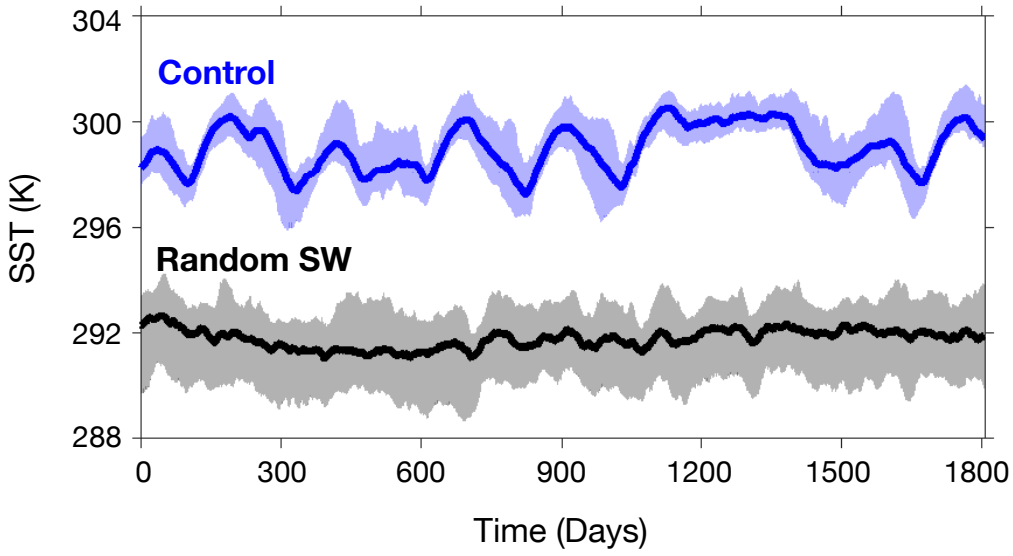

Figure S1. Timeseries of SST in the Control and Random SW simulations. Solid lines show the global-mean SST, and shading shows the interquartile range.

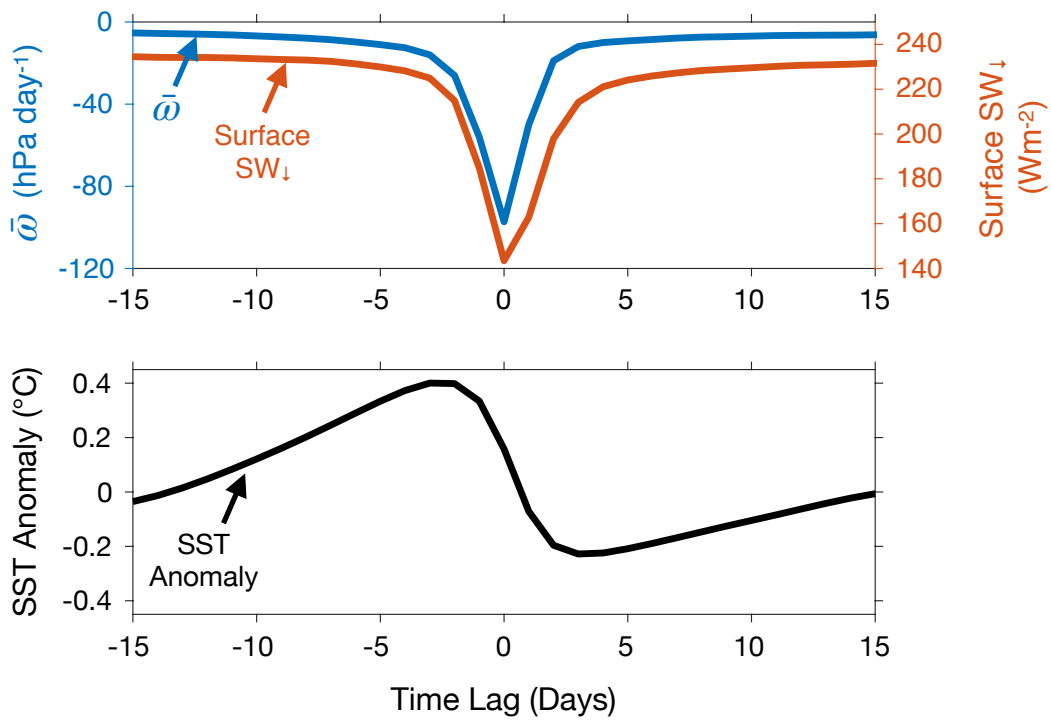

Figure S2. Demonstration of the cloud shading feedback in the Control simulation. Days of moderate-to-strong ascent are identified, and lead-lag composites centered on the time of peak ascent are shown. The upper panel shows column-average vertical motion ($\overline{\omega}$) and the downward SW flux at the ocean surface, and the lower panel shows SST anomalies.

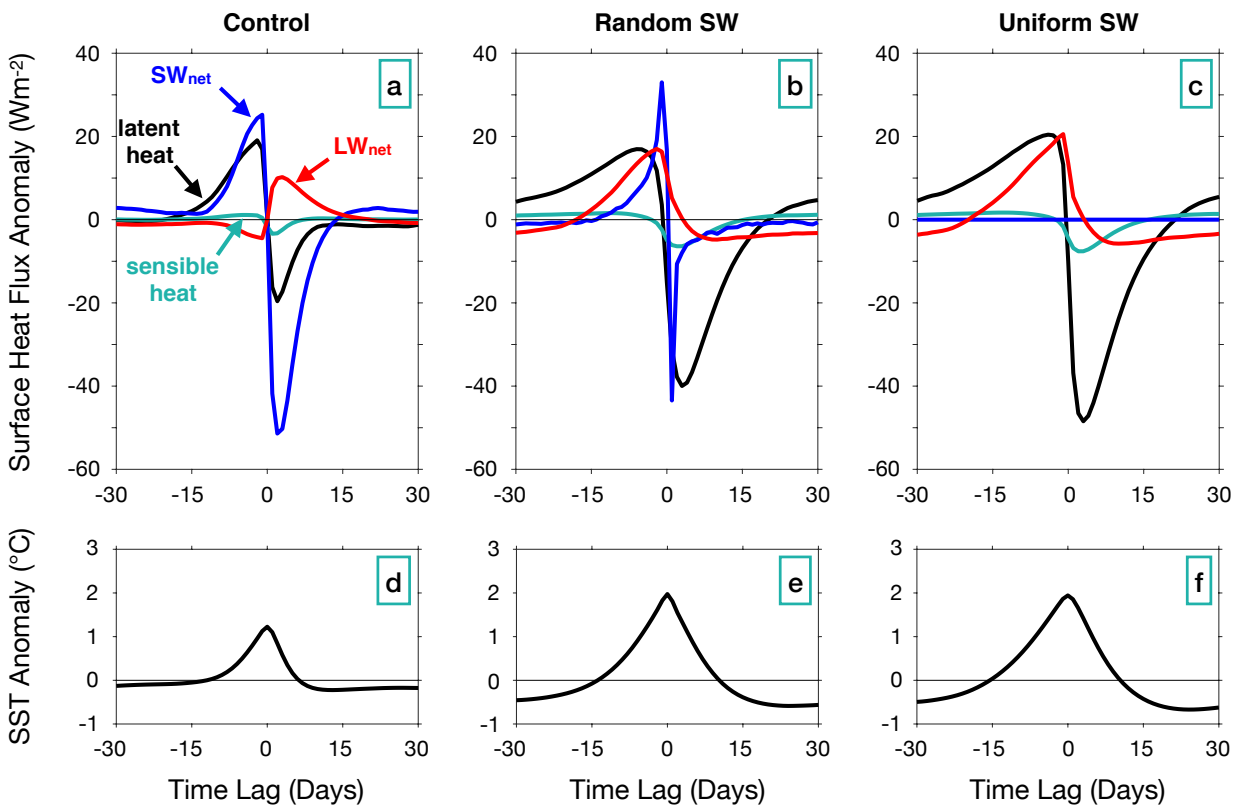

Figure S3. Surface heat budget and SST in the Control, Random SW, and Uniform SW simulations. All panels show lead-lag composites centered on warm SST events, which are defined as instances in which a warm SST anomaly that exceeds one standard deviation reaches its peak value. (a) Anomalies in the surface heat budget terms in the Control simulation, including net SW and net LW radiation, and latent and sensible heat flux. A positive anomaly for the surface heat fluxes indicates heating of the ocean. (b-c) Similar to (a), but for the Random SW and Uniform SW simulations, respectively. (d-f) SST anomalies for the Control, Random SW, and Uniform SW simulations, respectively.

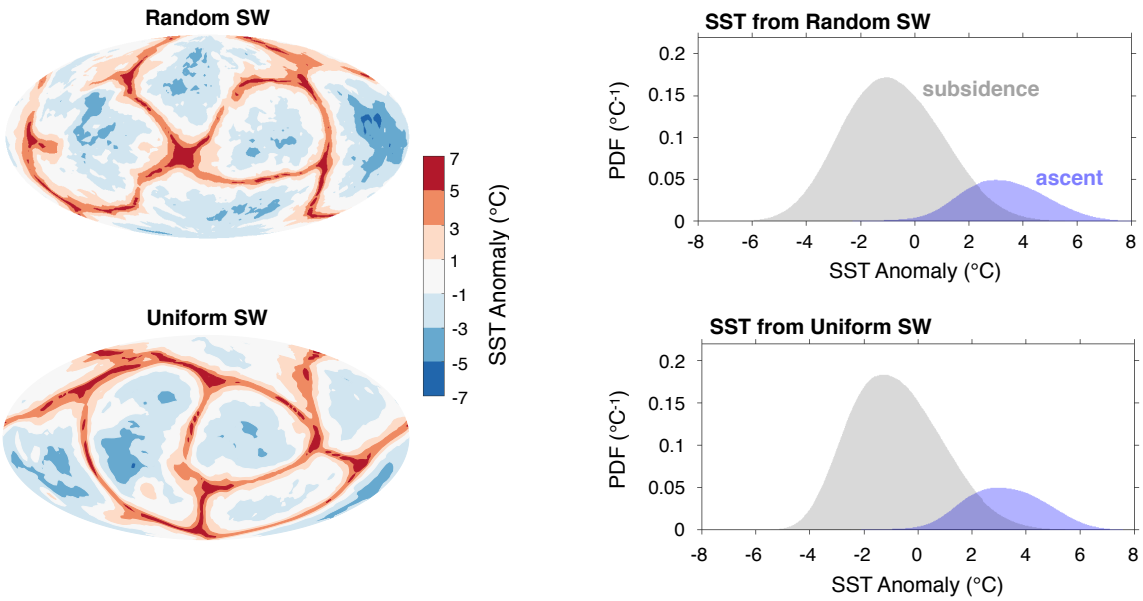

Figure S4. Comparison of SST in the Random SW and Uniform SW simulations. The left column shows snapshots from the simulations that reveal typical global SST patterns, and the right column shows the probability density function (PDF) of SST decomposed into contributions from grid points with net ascent and grid points with net subsidence in the troposphere. All figures show SST anomalies, which are computed by removing the global-mean SST from each simulation day.

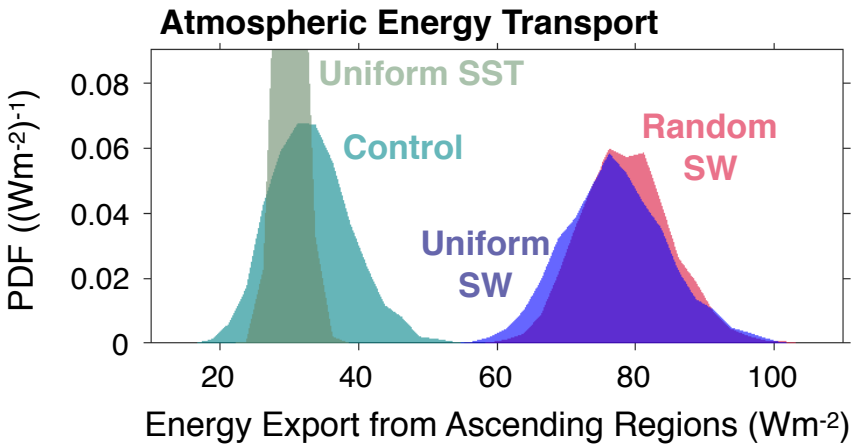

Figure S5. Energy exported horizontally from ascending regions by the atmospheric circulation. Each point in the histogram represents the average energy export from ascending regions during one simulation day. PDFs for all four simulations are shown.

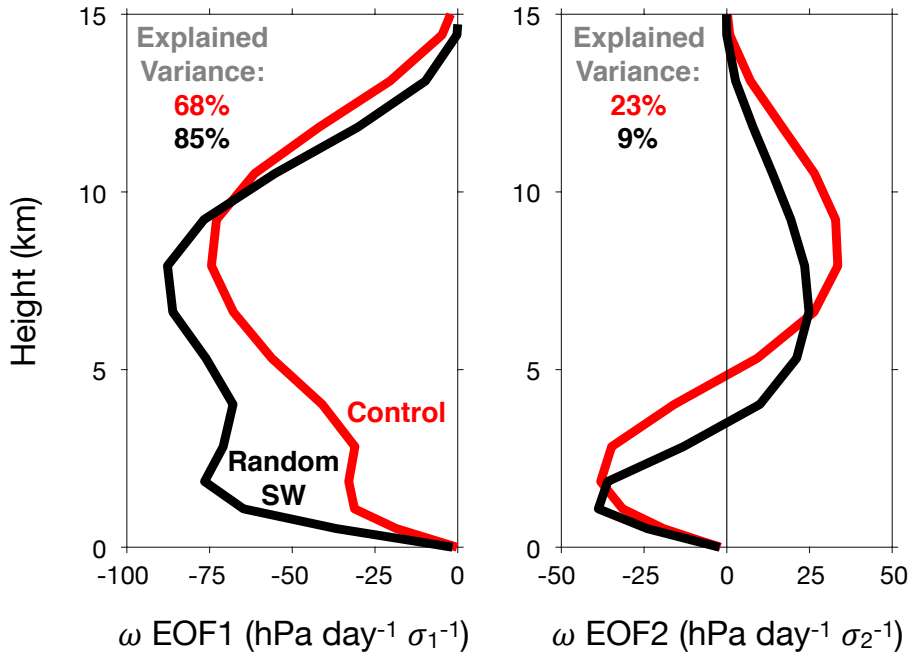

Figure S6. Common modes of variability of vertical motion. (left) The leading EOF of ω in the Control and Random SW simulations. The EOFs are expressed in units of hPa per day per standard deviation of the leading principal component (σ_1). The percentage of variance of ω that is explained by the leading EOF is indicated in the upper left corner. (right) Similar to the left panel, but for the second EOF.

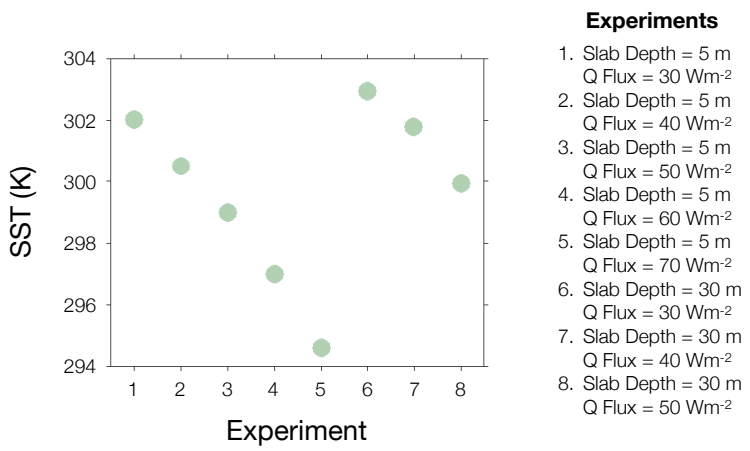

Figure S7. Global-mean SST in the Control simulations of the sensitivity study. Eight experiments were performed in which the slab ocean depth and Q flux were varied, as indicated in the list on the right. Experiment 3 is presented in the main text.

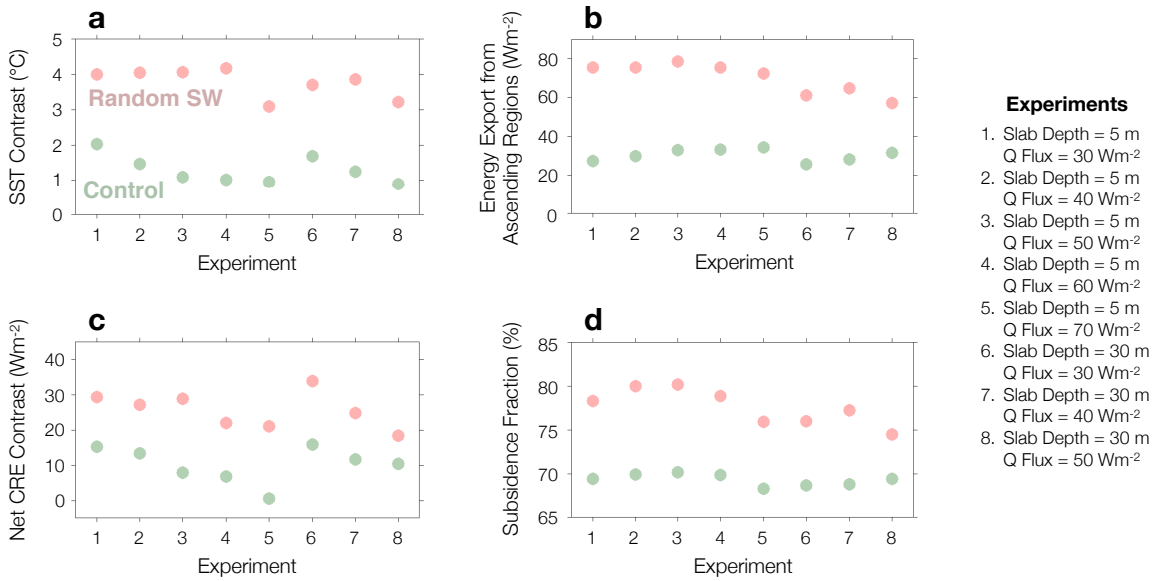

Figure S8. Results of the sensitivity study. The averages of several key variables are shown, including (a) the SST contrast between ascending and subsiding regions, (b) the net energy exported from ascending regions by the atmospheric circulation, (c) the magnitude of the net CRE contrast between rising and sinking regions, and (d) the subsidence fraction. Experiment 3 is presented in the main text.

	Control	Random SW	Difference
10 m Wind Speed (m/s)	3.4	5.2	+1.8
Subsidence Fraction (%)	70.1	80.2	+10.0
Surface Net SW Flux (W/m^2)	222.9	222.9	0
Surface Net LW Flux (W/m^2)	-67.4	-74.8	-7.4
Surface Latent Heat Flux (W/m^2)	-94.2	-85.4	+8.7
Surface Sensible Heat Flux (W/m^2)	-11.1	-12.6	-1.5
10 m Relative Humidity (%)	76.2	76.0	-0.2
Precipitation (mm/day)	3.3	3.0	-0.3
SST (K)	299.0	291.8	-7.2

Table S1. Global-mean climate metrics for the Control and Random SW simulations. For the surface heat budget terms, a positive value indicates heat flowing into the ocean.